SEDIMENTOLOGY the journal of the International Association of Sedimentologists

*Sedimentology* (2017) **64**, 609–630 doi: 10.1111/sed.12281

# A log-normal spectral analysis of inorganic grain-size distributions from a Canadian boreal lake core: Towards refining depositional process proxy data from high latitude lakes

PAUL R. GAMMON*†, LISA A. NEVILLE†[1], R. TIMOTHY PATTERSON†, MARTINE M. SAVARD‡ and GRAEME T. SWINDLES§

**Natural Resources Canada, Geological Survey of Canada, 601 Booth St, Ottawa, Ontario, Canada K1A 0E8 (E-mail: paul.gammon@canada.ca)*

*†Department of Earth Sciences, Carleton University, Ottawa, Ontario, Canada K1S 5B6*

*‡Natural Resources Canada, Geological Survey of Canada, Quebec City, Quebec, Canada G1K 9A9*

*§School of Geography, University of Leeds, Leeds, LS2 9JT, UK*

Associate Editor – Daniel Ariztegui

**ABSTRACT**

Better methods for interpreting grain-size spectra will enhance current understanding of past transport–depositional processes. A high-resolution inorganic grain-size dataset has been measured from a freeze core extracted from 'Alberta Lake E' a boreal fresh water lake 40 km east of the Athabasca Oil Sands in north-eastern Alberta, Canada. The grain-size spectra are remarkably consistent throughout the core, exhibiting a structure comprising six persistent grain-size distributions below *ca* 250 μm, plus a rare medium-sand distribution. Automated deconvolution of the grain-size spectra produced poor results. Constraining the modes of two of the distributions produced deconvolution solutions that were statistically excellent and consistent with the structure of each spectrum. Statistical analysis of the 'constrained' solutions indicates that deconvolution successfully extracted independent grain-size populations. Conversely, the multimodal spectra generate traditional measures (for example, mean grain size) that are inconsistent combinations of different individual populations and thus are poor proxies of transport–depositional processes. Alberta Lake E is situated in a boreal wetland landscape where sediment delivery is dominated by overland flow transport during spring melt. This context means that the Alberta Lake E grain-size spectra can be interpreted to reflect: (i) a bedload component transported during short-duration high discharge events that reflect the intensity of the melt; and (ii) a finer suspended load component representing material whose magnitude is controlled by the volume of the spring melt. Stratigraphically, bedload and suspended load populations demonstrate different short-wavelength and long-wavelength cyclicity, suggesting that spring melt is likely to be driven by cyclic external forcing factors. The links between the grain-size spectra and spring melt have potential for generating proxy records that better capture the external controls over spring melt in boreal systems and the risks associated with these energetic hydrodynamics. This is exemplified by the coarsest Alberta Lake E distributions, which indicate that more intense spring-melt dynamics occurred in pre-historical times.

[1]Present address: Natural Resources Canada, Geological Survey of Canada, Calgary, Alberta, Canada, T2L 2A7.

**Keywords** Boreal lake, grain-size analysis, parametric curve fitting, sedimentology, spring melt, stratigraphy.

## INTRODUCTION

A focus of palaeoenvironmental research is the development of high-resolution palaeoenvironmental reconstructions spanning the last few thousand years (PAGES_2k_Consortium, 2013). High-resolution studies generally require large numbers of analyses of samples that capture, generally via a proxy relationship, an environmental variable of interest. The advent of laser particle analysers (Syvitski, 1991) and microtomes (Macumber *et al.*, 2011) now makes it possible to rapidly generate high-resolution grain-size datasets from fine slices of unconsolidated sediment cores. However, the use of grain-size data as a temporal proxy for environmental processes remains controversial (Middleton, 1976; Flemming, 2007; Le Roux & Rojas, 2007; Weltje & Prins, 2007; Dietze *et al.*, 2012; Xiao *et al.*, 2012). Less controversial, although rarely utilized in palaeoenvironmental time series, is the recognition that most grain-size spectra are composites of multiple overlapping grain-size populations (Sheridan *et al.*, 1987; Qin *et al.*, 2005; Bartholdy *et al.*, 2007; Le Roux & Rojas, 2007; Xiao *et al.*, 2012; Dietze *et al.*, 2013). In such spectra, the identification of individual populations is reliant on statistical deconvolution. The most common methods proposed for deconvolving grain-size spectra are: (i) full discrete parametric curve fitting (e.g. Sheridan *et al.*, 1987; Qin *et al.*, 2005; Xiao *et al.*, 2012); (ii) end-member mixing analysis (EMMA; e.g. Weltje & Prins, 2007; Dietze *et al.*, 2012, 2013; Ijmker *et al.*, 2012); and (iii) sediment trend analysis (STA; e.g. Bartholomä & Flemming, 2007; Le Roux & Rojas, 2007; Poizot *et al.*, 2008). Both EMMA and STA have been used mostly to investigate grain-size distributions within a horizontal (single temporal timeframe) two-dimensional context, such as sedimentary facies distributions and their underlying generalized transport–depositional processes. Both of these geostatistical techniques assume that the grain-size distributions of different samples are a reflection of the transport–depositional processes within an area, i.e. the samples are assumed to be in a dynamic relationship and the algorithm employed seeks to uncover that relationship. This assumption is not necessarily valid in temporal studies, where the vertical 1D stratigraphy can capture diverse, unrelated sedimentological processes. Nevertheless, EMMA has been utilized in the analysis of the environmental processes linked to ancient sediments (Weltje & Prins, 2003; Dietze *et al.*, 2013).

In contrast to EMMA and STA, deconvolution via parametric curve fitting is based on the principle that any individual grain-size spectrum represents an amalgam of discrete grain-size populations, each of which was generated by an erosional–depositional–transport mechanism (Tanner, 1964; Ashley, 1978; McLaren & Bowles, 1985; McCave & Hall, 2006; Xiao *et al.*, 2012). Deconvolution procedures aim to identify all of the individual populations within each spectrum. The relative merits of a variety of parametric curve-fitting approaches have been debated at length (for example, tanh, log-normal, log-hyperbolic, Weibull functions, etc.; Bagnold & Barndorff-Nielsen, 1980; Påsse, 1997; Sun *et al.*, 2002; Leys *et al.*, 2005; Hajek *et al.*, 2010; Barusseau, 2011) and it is likely that the best parametric curve-fitting approximation is context specific. Barusseau (2011) summarized the debate well by differentiating between the end uses of grain-size deconvolution: (i) for disciplines such as hydraulic engineering and coastal geomorphology, the grain-size populations need to be deconvolved as accurately as possible because the defined population(s) will be used in subsequent models of sediment dynamics and engineering solutions. Given the complexities of real systems, the choice of parametric function for deconvolution needs to be carefully examined (Flemming, 2007; Molinaroli *et al.*, 2009; Barusseau, 2011); (ii) studies that compare grain-size populations (for example, sedimentary facies analysis or time series) are more concerned with variability within and between samples and, consequently, the choice of parametric curve type probably introduces at worst an internal and/or systematic error. The populations derived are, therefore, inferred to be internally consistent with a qualitative relationship to environmental processes. Nevertheless, some studies have further attributed the deconvolved populations to specific environmental processes

(Tanner, 1964; Ashley, 1978; McLaren & Bowles, 1985; McCave & Hall, 2006; Bartholomä & Flemming, 2007; Molinaroli *et al.*, 2009).

Relatively few time-series studies have utilized deconvolved individual grain-size populations (Chen *et al.*, 2013). Instead, time-series studies of grain-size data commonly utilize traditional grain-size summary statistics or specific components (for example, median or mean grain size, percent clay and/or silt and/or sand, end-member mixing proportions) and interpret these as proxy data for the general sediment dynamics (Wang *et al.*, 2006; Weltje & Prins, 2007; Johnson & McCave, 2008; Dietze *et al.*, 2012; Chen *et al.*, 2013). The implicit assumption when using these types of grain-size proxies is that they adequately represent environmental processes.

This study utilizes a novel deconvolution and peak-fitting procedure, which includes constraints on solutions, to extract unimodal log-normal grain-size populations for a subset of the grain-size spectra analysed from a sediment freeze core extracted from 'Alberta Lake E' (ALE); an informally named lake situated *ca* 40 km north-east of Fort McMurray, Alberta, Canada (Fig. 1). This sample subset is subsequently used as a training set to extend some deconvolved population parameters across the complete ALE grain-size data. The quantitative grain-size proxy data are then combined with a detailed understanding of the sedimentological and physiographic context of ALE to generate a stratigraphic profile of specific bedload and suspended load transport-deposition processes. The deconvolved populations are also compared against traditional proxy data measures such as mean grain size.


**Fig. 1.** Map of Canada with the province of Alberta (AB) and the approximate location of Alberta Lake E (ALE; arrowed black square). For details, see Fig. S1.

## METHODS

### Sediment collection

A 1·45 m freeze core was collected from Alberta Lake E (ALE) at 3·75 m water depth in September 2010 (latitude 56·87933°; longitude −110·5678°). The coring location was chosen based on water depth, location within the lake, surrounding landscape and substrate type. For further physiographic information on ALE, see Supplementary Information. The massive black gyttja sediment remained frozen until sectioning prior to grain-size and other analyses. The core has a $^{210}$Pb age model that indicates that the top 30 cm represents the last 150 years (Jautzy *et al.*, 2013).

### Grain-size measurements

A purpose-built freeze-core microtome was used to section the ALE core (mostly 1 mm resolution), starting with the 0 to 1 mm surface sample (slice 1) to slice 1451, with every second slice being analysed for grain size making a total of $n$ = 701 analyses. Detailed information regarding pre-analysis strategy and treatment methods is documented in the Supplementary Information. Briefly, sediment samples were digested in a heated water bath with 10% v/v% $H_2O_2$ to remove organics (van Hengstum *et al.*, 2007). Grain-size analysis of digested samples was performed in triplicate with a Beckman Coulter LS 13 320 Laser Diffraction Analyzer (Beckman Coulter Inc., Brea, CA, USA) fitted with a Universal Liquid Medium (ULM) sample chamber. The samples were run in distilled water with an obscuration level of 10 ± 3%, over a measurement range of 0·4 to 2000 μm (Murray, 2002). The laser diffraction data were initially converted to equivalent spherical grain-size volume using the Fraunhofer and Mie diffraction models, and then size-class data were averaged for the triplicate analyses. Gradistat software (Blott & Pye, 2001) was used to extract the mean grain size, medium silt, total silt and fine sand volume percentages from the equivalent spherical grain-size diffraction data.

 

## Grain-size data analysis

Multiple deconvolution methods were trialled (detailed in both the *Results* section below and Supplementary Information). The final deconvolution protocol used was as follows:

**1** All grain-size spectra were examined visually to determine the general structure of the spectra (Fig. 2) and to identify any spectra that did not conform to the general spectral structure (Fig. 3). See also Supplementary Information *Notes 1* and *2*.

**2** A subset of 50 samples was chosen for testing different deconvolution and peak-fitting combinations. These samples were spaced approximately every 200 mm down core, with at least three contiguous samples chosen from each 200 mm segment. The contiguous samples were specifically chosen to capture the grain-size spectral variability for that 200 mm portion of the core (Fig. 2). This selection method ensured that the sample subset included grain-size spectra that were broadly representative of both the whole core and the most important aspects of grain-size variability, including potential cyclic sedimentation processes.

**3** The second-order and fourth-order derivatives of each spectrum within the subset were calculated (Fig. 4) to help identify the positions of pop-

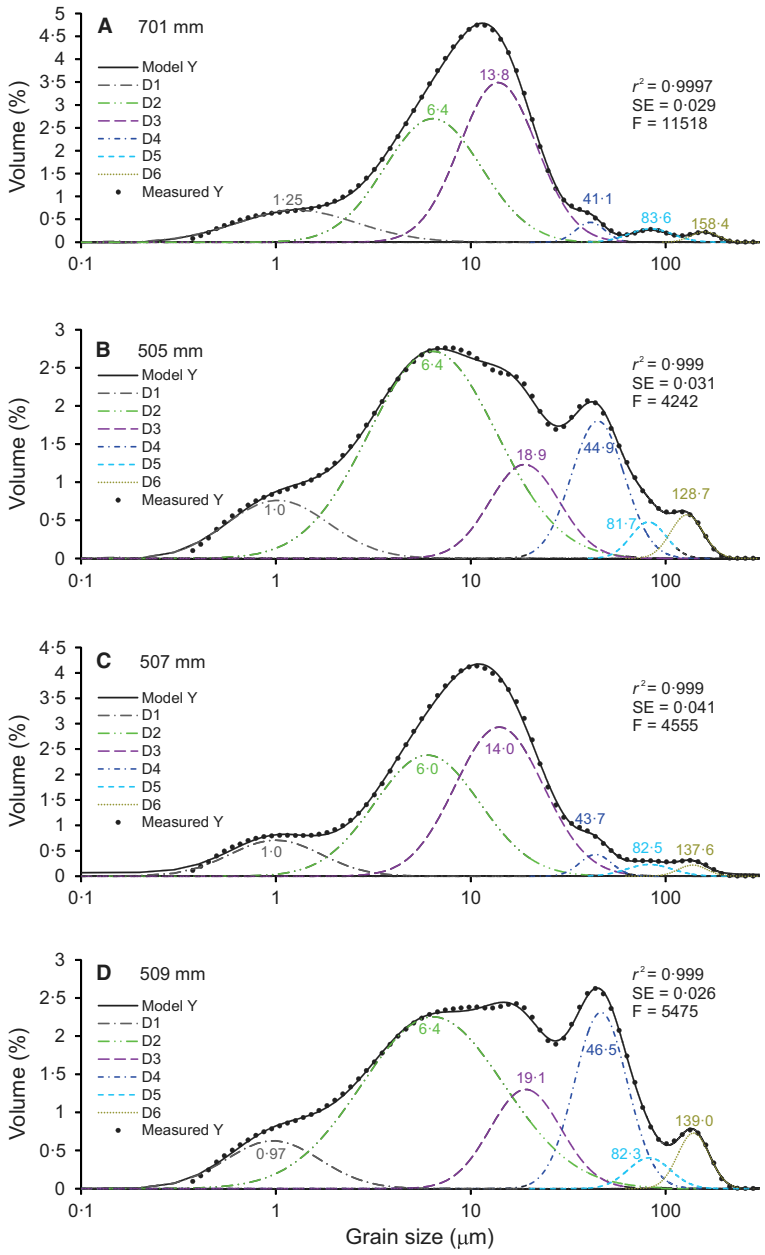


**Fig. 2.** Constrained deconvolved and peak-fitted grain-size spectra for the Alberta Lake E (ALE) freeze core. In each panel, the upper portion represents the actual distribution (dotted line) and its approximation (solid line) as the sum of the different log-normal distributions D1 to D6. Also noted are the modes of each peak, and the goodness-of-fit statistics [regression least-squares coefficient of determination ($r^2$), standard error (SE) and *F*-statistic, respectively]. (A) This sample has one of the finest grain-size distributions, with a single fine silt peak at *ca* 11 μm. (B) to (D) medium-grained (B), fine-grained (C) and coarse-grained (D) distributions in three contiguous samples. Similar grain-size spectral variation is present at all levels within the core.

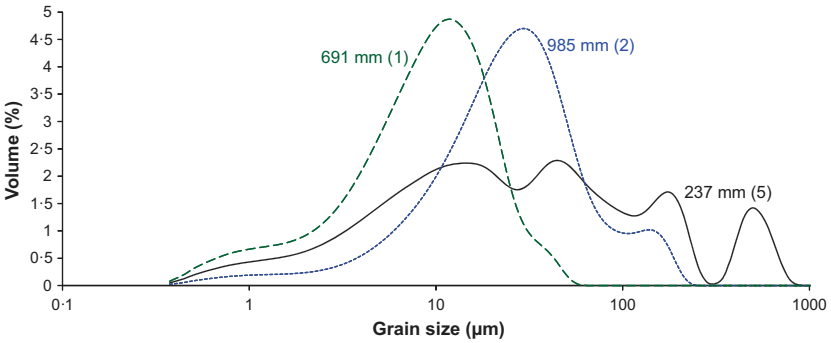


**Fig. 3.** Distributions of the three types of atypical grain-size spectra. The sample depth (in millimetres) refers to the core depth of the figured sample, while the bracketed number depicts how many of these spectra occur within the dataset.

ulations that are represented by either unambiguous peaks (i.e. peaks with two downward-sloping sides) or changes in slope (inflection points) that are likely to be indicative of the existence of subordinate grain-size populations within the spectrum (cf. Qin *et al.*, 2005; Bartholdy *et al.*, 2007; Flemming, 2007; Xiao *et al.*, 2012). The derivative plots also identify the approximate mode for each of the log-normal distributions, which was noted and used in later steps in the analytical process.

**4** The PeakFit® software package (SeaSolve Software Inc.; www.seasolve.com) was used to deconvolute each spectrum in the 50 sample subset. Initial trials used 2, 3, 4 … to 9 log-normal distributions. This trial and error aimed to determine the most suitable number of distributions for each spectrum, an approach also commonly employed in automated log-normal fitting (Xiao *et al.*, 2012) and EMMA (Weltje & Prins, 2007).

**5** Optimization of the log-normal distributions within each deconvolution model (termed peak fitting) was also conducted via PeakFit® software. PeakFit uses an iterative 'peak sharpening' (derivative-based) algorithm whereby a solution is derived and then tested to determine whether any further 'sharpening' produces better or worse least-squares criteria. The iterations were continued until the chi-square goodness-of-fit criteria attained values unchanging in the sixth decimal place. Once completed, the fit between the model and measured spectra can be evaluated via the coefficient of determination ($r^2$), standard error (SE) and *F*-statistic goodness-of-fit measures (Figs 2 and 3). Overall, each deconvolution and subsequent peak optimization (steps 4 and 5) procedure is similar to methods used by other authors undertaking log-normal deconvolution (Ashley, 1978; Sheridan *et al.*, 1987; Sun *et al.*, 2002; Qin *et al.*, 2005; Flemming, 2007; Xiao *et al.*, 2012).

**6** Peak fitting can generate incorrect results by migrating distributions to unrealistic values (Seasolve, 2003) which did occur in these peak-fitting models. To correct this problem, the mode of distribution 2 was constrained to between 5·0 μm and 6·5 μm and that of distribution 5 to >80 μm (the reasons for this are detailed in Supplementary Information *Note 3*).

**7** The reproduction of the basic spectrum structure (i.e. main spectral peaks and troughs align with the main distributions within a solution) was used as a qualitative criterion for acceptance or rejection of different deconvolution models.

**8** The deconvolved and peak-fitted model generates the following statistics for each identified log-normal distribution within a spectrum: area, maximum amplitude, modal grain size and the full-width at half the height of the maximum amplitude (FWHH, which is a similar measure to the standard deviation of a distribution).

### Extending the deconvolution to the other grain-size spectra

To extend the deconvolution analysis across the whole dataset, the 50 deconvolved samples were used as a training set to generate, via least-squares fitting, a polynomial that could estimate, using the size-class data of each grain-size analysis, the area and amplitude statistics for the remainder of the samples (using STATA® statistical software; www.stata.com). Algorithms were generated for the distribution 3 (D3) Area and distribution 6 (D6) Amplitude parameters (Supplementary Information; Appendix S1). These two examples were then compared with other grain-size measures, such as mean grain size.

## RESULTS AND INTERPRETATION

### Spectral Deconvolution

*Grain-size spectral structure*

The grain-size spectra from ALE are exceptionally consistent in their overall structure (Figs 2,

 

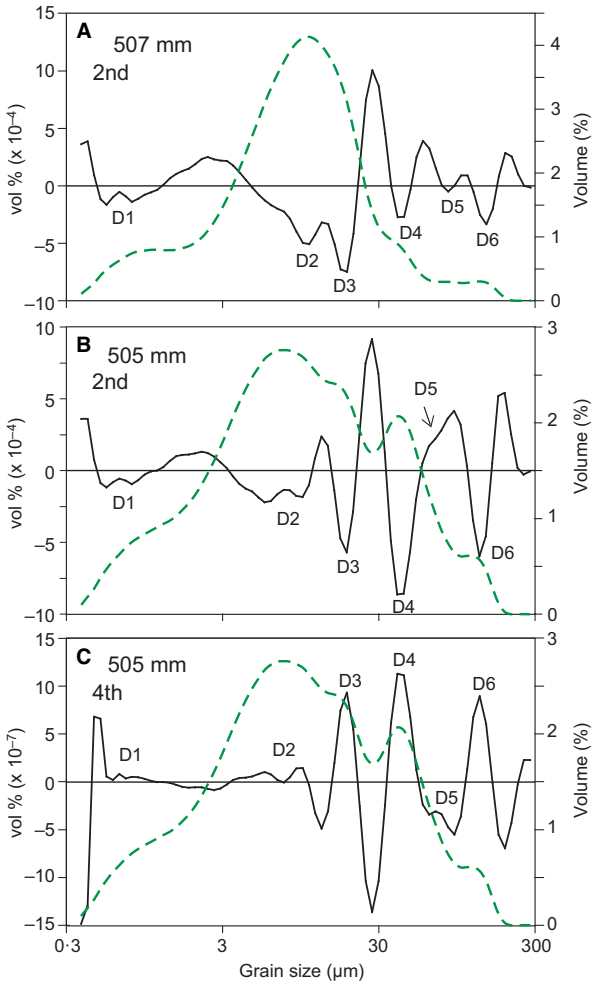


**Fig. 4.** Second-order and fourth-order derivative plots of two samples from Fig. 2. Solid lines mark the derivative curve with scale on the left-hand *y*-axis. Green dashed lines mark the original spectrum with scale on the right-hand *y*-axis. The positions of individual distributions are denoted by downward-facing peaks in second-order plots and upward-facing peaks in fourth-order plots: '2nd' and '4th' denote second-order or fourth-order derivative plots. (A) Second-order derivative plot of a fine-grained sample with six distributions. (B) Second-order derivative plot of a relatively coarse-grained sample with D5 denoted by an inflection. (C) Fourth-order derivative plot of the 505 mm sample of (B) where the D5 population denoted in the fourth derivative. Note that in all derivatives, the D1 peak is relatively small in comparison to a tall peak that is a computational artefact generated by the sharp cut-off at the lower limit of the grain-size analysis.

S4 and S5). From the finest grain size measured (0·4 μm) to *ca* 3 to 4 μm, there is a broad low-amplitude shoulder or unambiguous peak observed in all spectra (Fig. 2). The area of fine grain sizes between 3 to 4 μm and *ca* 30 μm contains either a single broad peak with a mode between 7 μm and 14 μm (Fig. 2A and C) or two clearly distinguished peaks with modes between *ca* 5·0 to 6·5 μm and *ca* 17 to 20 μm (Fig. 2B and D). Generally, samples characterized by overall coarser-grained spectra are those with two clearly distinguished peaks. Between *ca* 30 μm and *ca* 120 μm, there is generally a single peak centred around 50 μm. The peak is either approximately symmetrical if it is of high amplitude (Fig. 2D) or asymmetrical if it has unequal-sloped sides of low amplitude (Fig. 2B). In some of the overall finest-grained spectra (i.e. spectra where the 3 to 30 μm area is relatively large), this peak can be reduced to an inflection beside a large finer-grained peak at 3 to 30 μm (Fig. 2A and C). In these finest-grained spectra, a small distinct peak occurs at *ca* 90 to 100 μm. However, in most spectra, this peak is generally represented by either a broad plateau or shoulder in the *ca* 70 to 120 μm grain-size range (Fig. 2B to D). The coarsest-grained peak that is common to all of these spectra is centred at *ca* 150 μm. The finer-grained side of this peak is coincident with the *ca* 70 to 120 μm plateau/shoulder and is generally a low-angle slope. The coarser-grained side of the 150 μm peak has an exponential decay slope in virtually all spectra.

Visual examination had previously identified three spectral types (total of eight samples) that diverge from the above structure (Fig. 3). The most common difference (five samples) is the presence of a broad, low-amplitude medium to coarse sand-sized population (the '237 mm' sample type; Fig. 3, solid line). The 237 mm sample itself has 7·7% of its total grain-size population in this peak, while the other four samples within this group have <1% of their total population in this peak. Samples with a medium-sand peak otherwise exhibit all of the common spectral structural characteristics listed above. The medium-sand distribution does not overlap any of the finer-grained distributions. Consequently, it is both easily distinguished and too minor to have been included in the spectral deconvolution and peak fit modelling.

The 691 mm sample has virtually no sand, but otherwise follows the general spectral structure above. This leaves only two spectra ('985 mm' type spectra in Fig. 3) out of the total 701 spectra that substantially diverge from the general spectral structure. These two adjacent samples, at 985 mm and 987 mm downcore, exhibit no fine silt peak, but rather a single coarse silt peak at *ca* 35 μm, a grain-size region

that is either a spectral low or a shoulder to the *ca* 50 μm silt peak in all other spectra.

*Grain-size spectral structure – interpreting the number of distributions*

The second-order and fourth-order derivative plots are good indicators of the smallest number of log-normal distributions present (Fig. 4; see also Supplementary Information *Notes 1* and *2*). For example, in the most fine-grained spectra examined, there is generally an unambiguous peak indicative of a small very fine sand-sized population (mode 80 to 110 μm; Figs 2A and 4A). In coarser-grained spectra, this minor population can only be inferred on the basis of an inflection and/or shoulder and/or plateau in this region (compare Fig. 2A to D). Second-order and fourth-order derivative plots yield a weak to moderate peak in the very fine sand region (Fig. 4B and C), indicating the presence of a very fine sand-sized population that is essentially hidden by the larger amplitude peaks on either side in coarser-grained samples. The six common distributions observed in the spectral structure are therefore consistent with the six peaks observed within the derivative plots (Table 1).

The trial and error deconvolution and peak-fitting procedure used generated fitting statistics that reached their maxima ($r^2$, *F*-statistic) or minima (standard error) with a total of six distributions (Fig. 5). Any increase in the number of distributions modelled did one or more of the following: (i) not result in any significant improvement of the fit statistics, and sometimes resulted in a decline; (ii) PeakFit generated

**Table 1.** Basic statistics for area, amplitude, mode, FWHH (full-width at half the height of the maximum amplitude), amplitude/FWHH for D1 to D6 in the 'constrained' model solutions

| | Units | Average | Minimum | Maximum | SD |
|---|---|---|---|---|---|
| D1 Area* | % | 8·37 | 1·65 | 11·63 | 1·89 |
| D2 Area* | % | 29·57 | 7·61 | 44·13 | 8·16 |
| D3 Area* | % | 29·62 | 12·94 | 58·68 | 11·90 |
| D4 Area* | % | 18·42 | 3·77 | 31·51 | 8·94 |
| D5 Area* | % | 6·45 | 1·93 | 17·03 | 3·57 |
| D6 Area* | % | 7·56 | 2·38 | 16·83 | 3·66 |
| D1 Amp | % | 0·62 | 0·12 | 0·81 | 0·12 |
| D2 Amp | % | 2·07 | 0·59 | 2·90 | 0·47 |
| D3 Amp | % | 2·25 | 0·96 | 4·67 | 0·91 |
| D4 Amp | % | 1·50 | 0·32 | 2·70 | 0·76 |
| D5 Amp | % | 0·53 | 0·15 | 1·52 | 0·33 |
| D6 Amp | % | 0·63 | 0·19 | 1·45 | 0·33 |
| D1 mode (M1) | μm | 1·07 | 0·89 | 1·37 | 0·12 |
| D2 mode (M2) | μm | 6·13 | 5·56 | 6·48 | 0·27 |
| D3 mode (M3) | μm | 16·46 | 12·30 | 20·80 | 2·30 |
| D4 mode (M4) | μm | 45·47 | 35·42 | 49·54 | 2·93 |
| D5 mode (M5) | μm | 86·29 | 80·15 | 101·40 | 5·86 |
| D6 mode (M6) | μm | 145·03 | 130·20 | 183·57 | 11·71 |
| D1 FWHH | μm | 1·66 | 1·08 | 2·47 | 0·34 |
| D2 FWHH | μm | 11·55 | 6·60 | 17·27 | 2·22 |
| D3 FWHH | μm | 21·73 | 15·52 | 31·92 | 3·88 |
| D4 FWHH | μm | 29·67 | 16·63 | 51·67 | 7·74 |
| D5 FWHH | μm | 59·98 | 22·54 | 85·88 | 11·37 |
| D6 FWHH | μm | 64·73 | 48·71 | 136·44 | 13·27 |
| Aspect ratio 1† | % | 153 | 121 | 185 | 17 |
| Aspect ratio 2† | % | 189 | 108 | 267 | 35 |
| Aspect ratio 3† | % | 132 | 102 | 191 | 17 |
| Aspect ratio 4† | % | 65 | 40 | 117 | 16 |
| Aspect ratio 5† | % | 70 | 26 | 95 | 12 |
| Aspect ratio 6† | % | 44 | 33 | 74 | 6 |

SD = standard deviation. *An area calculation for these distributions has units of μm%, and here it is normalized against FWHH to render percentages comparable between the different distributions. †Aspect ratio of these distributions = width per micron grain size ~ FWHH # ÷ Mode # where # = distribution number. Subsequently converted to percentages.

 

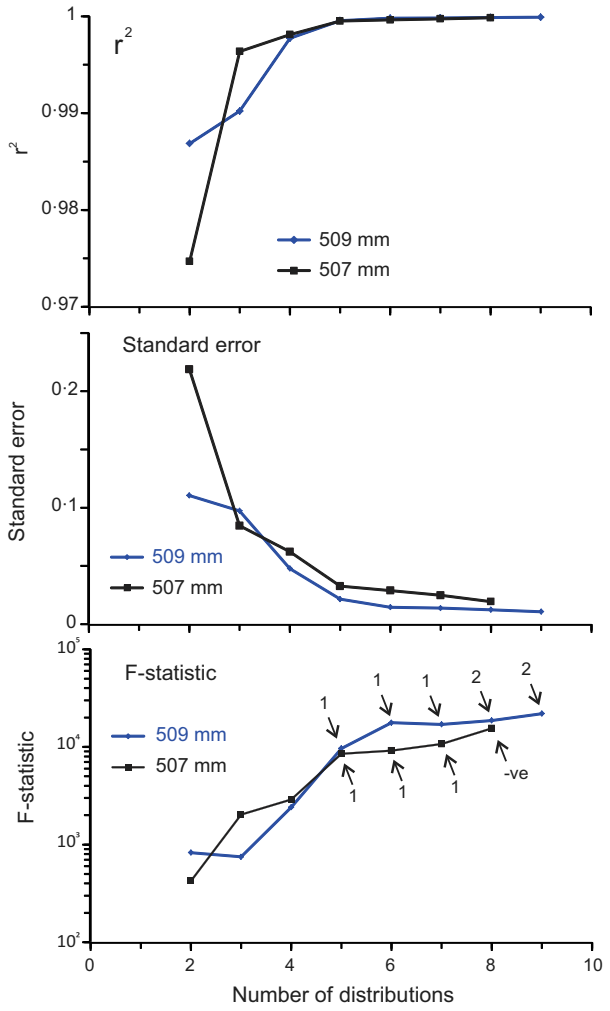


**Fig. 5.** Plot of fit statistics $r^2$, standard error and *F*-statistic for determining the most appropriate number of distributions in a model solution. Samples 507 mm and 509 mm were modelled using two to nine log-normal distributions and in this example unconstrained fully automated deconvolution and peak fitting. Substantial improvement in the fit statistics (an inflection point) stops at five distributions. However, at five distributions one distribution is wholly contained within another (annotated on the bottom plot are the number of such subservient distributions), indicative of the unrealistic solutions generated by 'unconstrained' fitting (see text). Once D2 to D3 and D4 to D5 separation is forced, the plots generate the inflection at six distributions. The '−ve' annotated on the bottom plot represents solutions with negative amplitude distributions. The constrained solutions for these samples are demonstrated in Fig. 2B and C.

near-zero or sometimes negative amplitudes for one or more of the distributions, indicating that the solution does not require those distributions to model the measured data; or (iii) one or more distributions was both wholly within and a minor component of another distribution, indicating that only one single distribution was required in that grain-size region (Fig S4B and S4C).

The general spectral structure (Fig. 2), derivative plots (Fig. 4) and deconvolved peak-fitted models (Fig. 5) all indicate that there are seven discrete log-normal grain-size distributions within these grain-size spectra. The subsequent modelling of these data utilized a six distribution structure to the PeakFit modelling (the six illustrated in Fig. 2, minus the rare '237 mm' type medium-sand mode distribution shown in Fig. 3). From smallest to largest, these distributions are termed D1 to D6 (see Table 1 for basic statistics). Similarly, the modes of these distributions are labelled M1 to M6, respectively.

Distributions D1 and D6, the finest and coarsest grain populations, respectively, are easily distinguished in virtually all spectra. Of the D2 to D5 distributions, the very fine sand distribution (D5) has unambiguous peaks in 45 (6·4%) of the spectra, the other three distributions all have unambiguous peaks in more than 20% of spectra; i.e. all of these distributions are common within the data. The only unambiguous peak excluded from the data is that at 35 μm in the two contiguous anomalous samples at 985 mm and 987 mm down core (0·3% of samples; Fig. 3).

## Peak fitting

### *Results*

Peak fitting generates the best statistical model without considering other constraints, such as spectral structure or derivative plots, and in an automated mode has a known tendency to migrate distributions (Seasolve, 2003). Peak fitting of the ALE grain-size data without any constraints on the distributions encountered this problem (see Supplementary Information *Note 3* for unconstrained peak-fitting results). To resolve this problem, without unduly limiting the potential peak-fitting solutions, required two constraints: (i) to force PeakFit to distinguish between the coarse silt and very fine sand distributions, the M5 (very fine sand mode) was constrained to >80 μm, consistent with the minimum M5 of 83·2 μm observed in the derivative plots (Fig. 4); and (ii) to force solutions to better approximate the bimodal structure of the 3 to 30 μm range, M2 was constrained to 5·0 to 6·5 μm. This range matched that observed in the

derivative plots (Fig. 4). The alternative of constraining the range of the M3 was trialled but found to be less successful, as gauged by generally poorer fitting statistics found with finer-grained samples. This was probably due to the best M3 estimate of 17 to 20 μm being derived from coarser-grained samples, which was probably an inappropriate M3 constraint for finer-grained spectra (Fig. 2; Table 1). Both the D2/D3 and D5 migration related issues are essentially a product of trying to find the best statistical model for strongly overlapping distributions, which is not a problem restricted to PeakFit or grain-size data and usually requires additional information to be fully successful (Flemming, 2007; Bah *et al.*, 2009). A statistical comparison between the unconstrained and constrained results is given in Supplementary Information *Note 4*.

Area and peak amplitude are measures of the overall size of the distribution (Hartmann, 2007), and the basic statistics for the constrained peak fits indicate that D2, D3 and D4 are the most important grain-size populations in these spectra (Table 1). In contrast, the mode and FWHH are measures that reflect the position and shape, respectively, of each distribution within a spectrum (Hartmann, 2007). Hence, the combined basic statistics of the deconvolution peak fit models (Table 1) are a representation of the position, shape and size of each distribution. These characteristics combined reflect the general spectral structure; that is, strongly overlapping D2 and D3; weakly overlapping D3 and D4; strongly overlapping D4 and D5; D1 and D6 weakly overlapping D2 and D5, respectively (Figs 2, 3 and S4). Both the FWHH and aspect ratio (mode-normalized FWHH) are measures of the distribution width, and both demonstrate the generally poor sorting for D1 to D3, moderate sorting for D5 and D6 and moderate to moderately well-sorted D4 (Table 2; Friedman, 1962).

Spearman's rank correlation analysis of the area, amplitude, mode and FWHH measures for the constrained model solutions provides an indication of how these parameters covary across the sample suite (Table 2). There are two striking features of the correlations between the size parameters of the distribution (Table 2A and B): (A) area and amplitude for D1 to D3 are negatively correlated with those of D4 to D6; and (B) area and amplitude for D4 to D6 are all strongly positively correlated with one another. Areas D1 to D3 exhibit no consistent cross-correlations with the only substantial correlation being a strong negative one between the D2 and D3 areas. The position (mode) and width (FWHH) of most distributions are generally uncorrelated (Table 2C and D). A notable exception to this is the positive correlation between mode and FWHH for D3 and D4.

*Interpretation*

Understanding the impact of constrained peak fitting is clearly important to the overall interpretation of these spectra. Constrained–unconstrained correlations indicate that the solutions for D4 and D6 are relatively robust irrespective of constraints, while all other solutions are variably impacted, D2 being the most impacted (see Supplementary Information *Note 3* for detailed discussion).

Log-normal distributions have long been recognized as an approximation of the individual grain-size populations, in that each log-normal distribution essentially reflects the transport-deposition processes that controlled that population (Middleton, 1976, 1990; Ashley, 1978; Flemming, 2007; Le Roux & Rojas, 2007; Xiao *et al.*, 2012). The strong positive and negative correlations between area and amplitude indicate fundamental scale-based relationships between the different populations within these spectra (Table 2). Scale parameters reflect the magnitudes of the different transport–depositional processes represented by the individual distributions (Hartmann, 2007), suggesting that there are important magnitude relationships revealed by this deconvolution methodology.

In contrast to the scale parameters, the position (mode) and shape (FWHH) parameters are a reflection of the hydraulic processes that govern the grain-size populations (Middleton, 1976; Sheridan *et al.*, 1987; Kranck *et al.*, 1996a,b; Påsse, 1997; Hartmann, 2007). The general non-correlation, with a notable exception of the D3 to D4 mode-FWHH relationships, of the position and shape parameters of these distributions indicates that for the most part, these populations are not generally linked at the hydrodynamic process level (Table 2). This suggests that the deconvolution and peak-fitting procedure used herein did successfully separate discrete grain-size populations that were each controlled by a distinctive set of erosion–transport–depositional processes (this is further examined in the *Discussion*). Overall, the area, amplitude, mode and FWHH parameters of grain-size distributions are important evidence for understanding the relationships between the different parameters, but are generally little used in stratigraphic studies utilizing grain-size data.

**Table 2.** Spearman's correlation coefficients for constrained log-normal distributions. (A) Area, (B) Amplitude, (C) Mode and (D) FWHH

| (A) | D1 Area | D2 Area | D3 Area | D4 Area | D5 Area | D6 Area |
|---|---|---|---|---|---|---|
| D1 Area | 1·00 | −0·23 | 0·23 | ***−0·44*** | *−0·25* | *−0·29* |
| D2 Area | 0·11 | 1·00 | ***−0·85*** | *−0·07* | *−0·16* | *−0·21* |
| D3 Area | 0·10 | <0·001 | 1·00 | *−0·32* | *−0·05* | *−0·19* |
| D4 Area | <0·001 | 0·61 | 0·02 | 1·00 | ***0·53*** | ***0·84*** |
| D5 Area | 0·08 | 0·26 | 0·73 | <0·001 | 1·00 | ***0·70*** |
| D6 Area | 0·04 | 0·14 | 0·19 | <0·001 | <0·001 | 1·00 |

| (B) | D1 Amp | D2 Amp | D3 Amp | D4 Amp | D5 Amp | D6 Amp |
|---|---|---|---|---|---|---|
| D1 Amplitude | 1·00 | ***0·63*** | −0·07 | ***−0·36*** | ***−0·40*** | ***−0·46*** |
| D2 Amplitude | <0·001 | 1·00 | −0·15 | ***−0·55*** | ***−0·53*** | ***−0·71*** |
| D3 Amplitude | 0·62 | 0·29 | 1·00 | ***−0·60*** | *−0·34* | ***−0·45*** |
| D4 Amplitude | 0·01 | <0·001 | <0·001 | 1·00 | ***0·61*** | ***0·84*** |
| D5 Amplitude | <0·001 | <0·001 | 0·02 | <0·001 | 1·00 | ***0·73*** |
| D6 Amplitude | <0·001 | <0·001 | <0·001 | <0·001 | <0·001 | 1·00 |

| (C) | D1 Mode | D2 Mode | D3 Mode | D4 Mode | D5 Mode | D6 Mode |
|---|---|---|---|---|---|---|
| D1 Mode | 1·00 | 0·04 | −0·18 | −0·03 | 0·15 | 0·31 |
| D2 Mode | 0·78 | 1·00 | ***0·48*** | 0·07 | 0·11 | 0·02 |
| D3 Mode | 0·22 | <0·001 | 1·00 | ***0·48*** | 0·18 | 0·07 |
| D4 Mode | 0·85 | 0·62 | <0·001 | 1·00 | 0·31 | 0·19 |
| D5 Mode | 0·29 | 0·45 | 0·21 | 0·03 | 1·00 | 0·32 |
| D6 Mode | 0·03 | 0·88 | 0·62 | 0·19 | 0·02 | 1·00 |

| (D) | D1 | D2 | D3 | D4 | D5 | D6 |
|---|---|---|---|---|---|---|
| D1 | 1·00 | ***−0·74*** | −0·16 | 0·04 | 0·14 | 0·42 |
| D2 | <0·001 | 1·00 | ***0·43*** | 0·28 | −0·08 | −0·02 |
| D3 | 0·27 | <0·001 | 1·00 | ***0·75*** | −0·02 | ***0·40*** |
| D4 | 0·81 | 0·05 | <0·001 | 1·00 | −0·13 | ***0·51*** |
| D5 | 0·32 | 0·60 | 0·89 | 0·38 | 1·00 | 0·30 |
| D6 | <0·001 | 0·90 | <0·001 | <0·001 | 0·03 | 1·00 |

Spearman's rank correlation coefficients are the numbers in the top-right half of the table, the corresponding statistical significance criteria are in the bottom left of the table, for example, distribution 3 to 4 area correlation is −0·32 at a significance of $P < 0·02$. Bold italics signify $P < 0·01$ level, while those in italics in 3A and 3B highlight the consistent negative correlation between peaks 1, 2, 3 and peaks 4, 5, 6.

### *Extending the deconvolution to non-deconvolved grain-size spectra*

The deconvolved and peak-fitted spectra represent a subset of the grain-size spectra measured in the study that are assumed to capture the spectral variability. The original grain-size frequency-class measurements were used as a training set against which the D6 Amplitude and D3 Area parameters were regressed as dependent variables to yield polynomial equations that approximate the deconvolution statistic (Fig. 6; Supplementary Information Appendix S1). The polynomial equations were used to extend the D6 Amplitude and D3 Area parameters across all samples except the two anomalous 'type 985 mm' spectra. The Spearman's rank correlation coefficients between the original deconvolution statistics and their polynomial approximations were 0·97 and 0·98 for D3 Area and D6 Amplitude, respectively.

## DISCUSSION

### Spectral deconvolution and peak fitting

The deconvolution of Alberta Lake E (ALE) grain-size spectra into seven distributions was

relatively straightforward due to the consistent stratigraphic spectral structure for all but two adjacent samples (Fig. 4). Conversely, peak fitting D1 to D6 of the spectra was not straightforward due to the degree of overlap between D1 to D3 and D4 to D5 distributions (Figs 2 and S4). As noted by many authors, there is no single solution when deconvolving and peak fitting strongly overlapping distributions within a spectrum, as also demonstrated by the excellent fit statistics for both constrained and unconstrained solutions (Ashley, 1978; Bagnold & Barndorff-Nielsen, 1980; Middleton, 1990; Påsse, 1997; Sun *et al.*, 2002; Flemming, 2007; Weltje & Prins, 2007; Bah *et al.*, 2009). Most grain-size deconvolution studies lack independent data for determining which peak-fitting solution is best, as is the case for ALE. Consequently, choosing a preferred peak fit is a subjective judgment based on a prioritization of the accuracy and importance of the different pieces of quantitative information within one or more spectra. The preferred solution is that which most accurately recreates the highest priority piece of quantitative information (Leys *et al.*, 2005). For the overlapping D1 to D3 and D4 to D5 grain-size ranges in the ALE spectra, the preferred solution was the one that reproduced the D2 and D5 modes exhibited in spectra hosting unambiguous D2 and D5 peaks. There is considerable sedimentological support for using the mode as the determining factor for anchoring grain-size population positions (Bah *et al.*, 2009; Barusseau, 2011; Kranck *et al.*, 1996b; Påsse, 1997; Sheridan *et al.*, 1987; and the many references therein). There is also mathematical support for prioritizing the distributional mode as the most accurate quantitative information when deconvoluting grain-size data (Lwin, 2003; Leys *et al.*, 2005; Weltje & Prins, 2007; Hajek *et al.*, 2010). Both of these lines of support highlight the mode as the single positioning parameter within both log-normal and other parametric curve-fitting approaches. In relation to peak fitting and the potential migration of modes to unrealistic values, the best summary encountered is: "It is therefore especially important that centre values be constrained and not be permitted unlimited freedom of movement" (the term 'centre' indicates mode; Seasolve, 2003). Many grain-size deconvolution and peak-fitting studies do not constrain the modal position, although the capacity to constrain modes in end-member mixing analysis (EMMA) is a notable exception (Weltje & Prins, 2007; Dietze *et al.*, 2012).

## Conceptual sedimentological context for Alberta Lake E

An understanding of the sedimentological context of Alberta Lake E (ALE) is required to assess the significance of both the observed grain-size populations and their stratigraphic variation. The first-order factors controlling ALE sedimentology include: (A) the hydrological regime controlling the run-off volume and intensity; (B) the climatic regime, which for this area is primarily the distribution of water through the seasonal cycle; (C) the landscape surrounding ALE, which controls the erosion-transport parameters; (D) the current action within the lake, which controls the internal distribution and/or redistribution of the grains entering the lake; (E) bioturbative mixing – being massive black gyttja, the ALE core would ordinarily be assumed to be pervasively bioturbated. However, there is a lack of fine-grained sand in the '691 mm' type sample, even though there are normal amounts of fine sand in the spectra of samples at 689 mm and 693 mm. Similarly, 2 mm spaced samples on either side of the five '237 mm' type samples contain no medium sand. This suggests a bioturbation mixing depth <2 mm; and (F) the grain-size distribution and mineralogy of the source regions, which controls what grain sizes are available for erosion–transport–deposition. Specific grain-size data for the source regions within the Fort McMurray area are limited to coarse size-class data, which indicates that all class sizes are available (appendix 4 of Andriashek, 2003; see also McLaws, 1980). The surficial geology of the area primarily comprises tills, which in general contain a wide variety of grain sizes. It is, therefore, considered unlikely that there is a deficiency in any particular grain-size class within the source region, and criterion '(F)' is not considered to have been a controlling factor in the ALE grain-size spectra.

The hydrological record indicates that the ALE region hosts a typical hydrological cycle for a boreal region (see *Physiography* section in Supplementary Information). The ALE coring site is also fully surrounded by wetlands (see Supplementary Information), and run-off of all types will have first traversed the wetlands before entering ALE. In boreal wetland environments, the seasonal hydrological pattern is markedly partitioned (Pomeroy *et al.*, 2007; Fang *et al.*, 2010; Shook *et al.*, 2013). Spring melting generates overland flow due to frozen subsurface organic soils that prevent or severely

 

inhibit infiltration of the large volumes of snow melt water that is delivered over relatively short time spans (Carson *et al.*, 1973; Gibson *et al.*, 1993; Metcalfe & Buttle, 1999; Gray *et al.*, 2001; Shook *et al.*, 2013). Sedimentological measurements of spring run-off indicate that the discharge volume generally controls the volume of sediment delivery (Metcalfe & Buttle, 1999, 2001; Laudon *et al.*, 2007; Cockburn & Lamoureux, 2008a,b), while the run-off 'intensity' (i.e. velocity and run-off rate) controls the delivered grain size (McDonald & Lamoureux, 2009; McDonald *et al.*, 2010). Combined, these studies demonstrate that the spring melt is a heterogeneous period that mostly comprises short peak-flow time periods, interspersed within and succeeded by recessional streamflow of significantly lower discharge volume and velocity. Commonly, the peak-flow events during spring melt are short-duration high discharge events driven by a rain and/or high temperature event (see fig. 5 in McDonald & Lamoureux, 2009).

In contrast, the summer–autumn–winter period is dominated by plant evapotranspiration and/or ongoing subsurface flow. During summer, boreal slope soils are mostly dry and take considerable wetting before they export water (Gibson *et al.*, 1993; Redding & Devito, 2008), while the wetlands act as a sink for precipitation (McNamara *et al.*, 2005; Kværner & Kløve, 2008; Redding & Devito, 2008; Lyon *et al.*, 2012). Nevertheless, summer thunderstorms are a component of northern boreal summers and represent a potential mechanism for overwhelming the holding capacity of the wetland and thereby initiating surface run-off (Kværner & Kløve, 2008). Redding & Devito (2008) estimated that for northern Albertan hill slopes, such as those of the Firebag Hills Uplands near ALE, the return period for summer storms capable of generating >1 mm of surface run-off (i.e. very minor flow) from the soil was *ca* 25 years. Wetlands would probably further attenuate the volumes and velocities of storm-generated summer–autumn run-off, thereby extending this return periodicity significantly (i.e. even anomalously large summer storm streamflow events would be strongly attenuated and not produce significant run-off into a wetland-surrounded lake such as ALE). Overall, it is highly likely that summer surface run-off to ALE is negligible for the majority of years. However, if summer run-off were to occur, the wetlands surrounding ALE would probably preferentially capture bedload and thus skew the sediment delivery to suspended load material. A grain-size spectrum similar to that of the '691 mm type' sample in Fig. 3 may reflect such a situation.

Easterly winds greater than 15 m $s^{-1}$ over the 1 km fetch between the eastern shore of ALE and the coring site could conceivably generate high-frequency wind waves *ca* 10 cm high (Hamilton & Mitchell, 1996; Young & Verhagen, 1996). However, the wind record for the region indicates that easterly winds of speeds above 8 m $s^{-1}$ are rare for the area. Case studies of lake high-frequency wind waves indicate a lack of reworking in benthic sediments at 3·5 m water depth (Luettich *et al.*, 1990; Jin & Ji, 2004; Hofmann *et al.*, 2008). Combined flow in lakes is generally generated via the coupling of inflow, outflow and wind. Much of the non-wave current activity is secondary effects of the waves and inflow regimes themselves (for example, reflected waves and coriolis circulation, Jin & Ji, 2004; Soulsby *et al.*, 1993). The limited fetch and seasonally restricted run-off period of ALE make it unlikely that combined flow is significant outside of the spring-melt run-off period. The floating riparian fen that rims the ALE shoreline attests to the lack of significant wave and current activity in the lake. Factor 'D' is therefore considered insignificant for a small lake, such as ALE, which is consistent with findings elsewhere.

The physiography surrounding ALE indicates that inorganic sediment will be derived from the northern hills and southern margins, plus potentially from the west, and delivered via the inlet channel (see Supplementary Information, Fig. S1). The stream channels entering ALE are all either well north-east (downstream and across the lakebed subaquatic channel) of the coring site or discontinuous wetland channels. The single inlet channel to ALE, which is near the coring site, and thus potentially an important sediment delivery system, is both discontinuous and embedded within extensive aquatic vegetation (reeds). It is probably a sink rather than a conduit, certainly for bedload particles. Overall, the lack of effective streams near the coring site means that focused point-source sediment delivery via stream channels is likely to be an insignificant method of bedload sediment delivery to the ALE coring site. Spring-melt overland flow, which has been demonstrated to be the predominant method of surface water flow across frozen wetlands (Gibson *et al.*, 1993; Metcalfe & Buttle, 1999; Shook *et al.*, 2013), is considered the most important sediment delivery mechanism to ALE.

As they apply to ALE, hydrology (factor A above), seasonal climate (factor B) and landscape characteristics (factor C) can be mostly considered to predominantly reflect the sediment delivery associated with the spring melt, as has been found for other boreal lakes (Carson *et al.*, 1973; Metcalfe & Buttle, 1999; Gray *et al.*, 2001; McNamara *et al.*, 2005; Laudon *et al.*, 2007; Redding & Devito, 2008, 2011; Fang *et al.*, 2010; Lyon *et al.*, 2012). Thus, the grain-size parameters identified within these spectra can be considered to be indicators or proxies for spring-melt sediment dynamics.

## Alberta Lake E grain-size populations – interpretation of processes

The ALE grain-size spectral structure is consistent throughout the entire core (Figs 2 and S5), suggesting that the seven log-normal distributions (six consistent, one rare) represent a suite of independent grain-size populations and processes that were persistent throughout the time period represented by the core. However, associating individual grain-size populations with specific processes is difficult and prone to error without corroborating process-based data. Nonetheless, the conceptual sedimentological framework above provides some limits as to what the grain-size analysis herein may represent (see also Supplementary Information *Note 5*). Distribution D1 is consistent with clay-sized suspended load material. The unique sedimentological properties of clay enable some confidence in its definition (McCave *et al.*, 1995a; Johnson & McCave, 2008; Xiao *et al.*, 2012). Distribution D2 is probably inorganic long-term suspended load material (Slattery & Burt, 1997; Chang *et al.*, 2006, 2007; Law *et al.*, 2008). The D1 and D2 distributions are both likely to be influenced by dissociation of aggregated flocs or particles during laboratory analysis, although the pre-treatment methods used here were designed to minimize this effect (see Supplementary Information; McConnachie & Petticrew, 2006). The strong positive correlation between D1 and D2 amplitudes (but not areas) indicates that there is some correspondence between the magnitudes of these two populations (Table 2). However, the non-significant mode correlation and strong negative correlation for D1 and D2 FWHH statistics suggest that these populations do represent different suspension processes (for example, low-density clay flocs versus mineral grains kept in suspension via turbulence).

Distribution D3 covers the size range for 'sortable silts' which have received considerable research attention (see Hamm & Dade, 2013). These are thought to be silt-sized grains that travel close to the bed under relatively low shear stress (McCave *et al.*, 1995b; Chang *et al.*, 2007; Johnson & McCave, 2008; Law *et al.*, 2008; Molinaroli *et al.*, 2009; Hamm & Dade, 2013). Turbulence in the bed boundary layer keeps these particles in suspension, and they undergo progressive sorting as flow decelerates (Middleton, 1976; McCave *et al.*, 1995b). The moderate mode and FWHH correlations between D2 and D3 indicate that a portion of the D2 grains was potentially travelling as sortable silt-sized aggregates that were disaggregated post-deposition, as has been observed elsewhere (Table 2; Supplementary Information; Chang *et al.*, 2006).

Distribution D4 is moderately to moderately well-sorted, suggesting that these grains were probably influenced by progressive sorting and are therefore likely to be bedload transported particles. It is the most consistent of all the populations with a relatively narrow range of modes, aspect ratios and FWHH statistics (Table 1). The strong spectral minimum between D3 and D4 probably demarcates the boundary between suspension and bedload sedimentology. Process-based studies indicate that the finest-grained bedload population is generally related to saltation processes (Middleton, 1976; Ashley, 1978; Singer & Anderson, 1984; Sheridan *et al.*, 1987; Chang *et al.*, 2006; Law *et al.*, 2008; Barusseau, 2011; Hamm & Dade, 2013). Distributions D3 and D4 have significant positive correlations between their position and shape parameters (mode and FWHH; Table 2C and D), suggesting that the sedimentological processes controlling these two populations are related; this is consistent with both being related to benthic boundary layer turbulence, which strongly controls the transport and progressive sorting of both sortable silt and saltating particles (Singer & Anderson, 1984; Hamm & Dade, 2013).

Singer & Anderson (1984) documented four populations within bedload transport that in order of increasing grain size were: (i) 'intermittent suspension' (equivalent to what nowadays would be considered suspended load sortable silt rather than bedload); (ii) saltation; (iii) finer-grained traction population; and (iv) coarser-grained traction population. These authors demonstrated that the relative magnitude of these bedload populations varies dependent on the transport conditions, but for bedload

sediment, undergoing progressive sorting in a decelerating flow the relationship is saltation > coarser-grained traction population > finer-grained traction population. The relative abundance of the bedload populations at ALE is similar with D4 > D6 > D5. It is consistent with bedload delivery to the ALE coring site probably being decelerating nepheloid layers (discussed further below; Chambers & Eadie, 1981; Singer & Anderson, 1984; Best *et al.*, 2005; Cockburn & Lamoureux, 2008b). In this context, D5 and D6 are both likely to be traction processes (for example, perhaps rolling versus sliding).

## Alberta Lake E grain-size record

The sedimentological context of ALE indicates that the ALE situation is a relatively simple particle delivery system dominated by the hydrological dynamics of spring melt. This simplicity is probably a primary reason why the spectral structure is so remarkably uniform throughout the core.

Bedload delivery of inorganic sediment (D4 to D6, plus medium sand D7) predominantly occurs during the high-energy events within the spring melt, which generally occur during the earlier portions of the nival period (McDonald & Lamoureux, 2009; McDonald *et al.*, 2010). Therefore, the D4, D5 and D6 spectral measures (mode, amplitude, area and FWHH) can conceptually be considered as proxy measures of different aspects of the spring thaw intensity. For example, the magnitude parameters area and amplitude of log-normal grain-size populations are generally interpreted as a proxy for the sum energy of the process (or processes) that gave rise to that grain-size distribution (Middleton, 1976; Ashley, 1978; Tanner, 1983; Syvitski, 1991; Kranck *et al.*, 1996a; Molinaroli *et al.*, 2009). The year 1990 hosted a high nival peak streamflow (Fig. S2B), which by this conceptual framework should equate to a relatively high D6 Amplitude in contrast to 1991, which should conceptually equate to a relatively low D6 Amplitude. The $^{210}$Pb age model for ALE (Jautzy *et al.*, 2013) does indeed suggest that this is the case (Fig. 6A). The age model also indicates that the regional floods of 1979 and 2007 seem to be represented by anomalously high D6 Amplitude values (maximum streamflows at the Clearwater above Christina station of 366 $m^3 s^{-1}$ and 299 $m^3 s^{-1}$, respectively). However, the highest values for D6 Amplitude occur deep in the core, suggesting that for the Oil Sands area, there is the potential for higher intensity spring-melt conditions than captured by current instrumental records.

The finer-grained suspended load populations (D1 to D3) are probably deposited throughout the overland-flow period (Metcalfe & Buttle, 1999, 2001; Laudon *et al.*, 2007; Cockburn & Lamoureux, 2008a,b). Overland flow occurs in both the nival run-up and through the earliest portions of the recession, eventually ceasing as the wetlands change from being a zone of bypass to a zone of attenuation for overland flow. Conceptually, there should be a relationship between run-off volumes and D1 to D3 population parameters. However, there is no difference between the D3 Area values for 1990 versus 1991, and these values are only slightly lower than that of the 1979 flood year (Fig. 6E). Given the conceptual framework and the recessional curves (Fig. S2B), the similarity of the D3 Area between these three years could qualitatively be assessed as due to similar volumes of run-off occurring in each of those years. The changing wetland dynamic, from sediment bypass to sink, is a function of wetland thaw rate and can be highly variable from year to year (Fang *et al.*, 2010). This change is not captured by any instrumental record; hence, an accurate calibration of the D1 to D3 parameters against instrumental run-off volumes is not currently possible. It would require quantitative data on the mechanics and timing of the wetland bypass to sink transition. Nonetheless, the correlations between the D1 to D3 population measures do suggest that these are proxy measures of spring thaw discharge volume, and their stratigraphic series thus provide a relative measure of the variability of spring thaw discharge volume.

The consistency of the spectral structure, plus the observed correlations between the distributions, indicates that the stratigraphic succession of D1 to D6 parameters reflects relative changes in the spring-melt depositional processes in ALE. As examples, Fig. 6 plots D6 Amplitude and D3 Area measures, as approximated using the polynomial equations, through the whole core (Appendix S1). These two parameters vary differently throughout the core (as also indicated by their non-correlation; Table 3). For example, the nine-point average value of D6 Amplitude decreases substantially down core from 0 mm to *ca* 600 mm, while there is essentially no change in D3 Area over the same interval. Conversely, there are substantial increases and decreases in the moving average of the D3 Area (a relative

**Table 3.** Spearman's rank correlation coefficients for calculated grain-size population variables D6 Amplitude and D3 Area against conventional summary statistics: mean grain size, total silt, medium silt and fine sand.

| | Mean GS (μm) | Fine Sand (vol%) | Medium Silt (vol%) | Total Silt (vol%) | D3 Area | D6 Amplitude (vol%) |
|---|---|---|---|---|---|---|
| (A) Spearman's rank correlation coefficients for individual sample data | | | | | | |
| D3 Area | 0·38 | *0·00* | 0·77 | 0·54 | 1·00 | *−0·09* |
| D6 Amplitude (vol%) | 0·79 | 0·96 | *−0·02* | −0·80 | *−0·09* | 1·00 |
| (B) As for (A) plus using a nine-point moving average to smooth the sample data | | | | | | |
| D3 Area | 0·39 | *0·03* | 0·88 | 0·63 | 1·00 | *−0·04* |
| D6 Amplitude (vol%) | 0·85 | 0·98 | *−0·04* | −0·71 | *−0·04* | 1·00 |

All correlation coefficients are statistically significant at $P < 0{\cdot}01$ except for those in italics. GS = grain size; vol % = volume percent.

proxy for spring-melt volume) in the bottom half of the core, an interval where D6 Amplitude (which represents nival peak flow) is relatively stable. This suggests that these two proxies include long-wavelength oscillations.

Superimposed on the longer wavelength oscillations are distinct shorter-wavelength oscillations (for example, *ca* 300 to 600 mm down core; Figs 6 and S5), indicating that spring-melt processes are considerably more variable in times past than for the more recent upper *ca* 200 cm (Fig. S5). This can also be seen in Fig. 2B to D, which demonstrates three adjacent grain-size spectra that represent a single high-amplitude and high-frequency cycle at *ca* 500 mm down core (see also Fig. S5). The variability in both short-wavelength and long-wavelength cyclicity of these spring-melt proxy measures probably reflects an overarching climatic control on the spring-melt dynamics, as has been found in other studies (e.g. Campbell, 1998; Cockburn & Lamoureux, 2007; Holz *et al.*, 2007; Fisher, 2011; Anderson, 2012; Dietze *et al.*, 2013). If so, this would imply that the climate mechanisms that control the spring melt are important for understanding the hydrological cycle of the area, including the environmental risks that the high-frequency oscillations and long-term average changes of these proxy data pose to the region.

## Grain-size populations versus traditional grain-size measures at Alberta Lake E

In depth or time-series analysis of grain-size proxy data it is implicitly assumed that the grain-size measure used is related to the depositional environment in a systematic relationship. For example, a common measure used is mean grain size, which is inferred to be the average of the depositional processes for the time period encompassed by the sample (two of many examples are Chen *et al.*, 2013; Sonnenburg *et al.*, 2013). Stratigraphic variation of the proxy data is further inferred to be a measure of the variation of the depositional processes over time. The process variables generated through the deconvolution and peak fitting, and their subsequent approximations across the whole dataset, can be compared against more traditional grain-size proxy measures such as mean grain size, total silt, etc. The grain-size range of the D6 population closely corresponds to that of the fine sand population, and there is minimal overlap of the D6 population with the D5 and D4 populations. This somewhat unlikely coincidence means that the fine sand component of the original grain-size data should correlate well with D6 Amplitude, which it does (Table 3; Figs 6A, 6B and 7A).

The grain-size range of D3 approximates that of fine plus medium silt (8 to 32 μm), plus a small contribution from very fine silt. There are no traditional grain-size measures that approximate this range, the closest being fine or medium silt measures. A more nuanced but still traditional approach could be to sum the size-class data for 8 to 32 μm, although the fine silt region of strong overlap between D2 and D3 means that the size-class data in this region are inherently a multi-distributional composite. Taking medium and total silt as standard traditional summary measures is clearly insufficient because both of these correlate relatively poorly with the D3 Area at the individual sample level and only modestly using a nine-point smoothing average (Table 3, Figs 6D, 6E, 6F and 7C). Comparing D3 against fine plus medium silt does

 

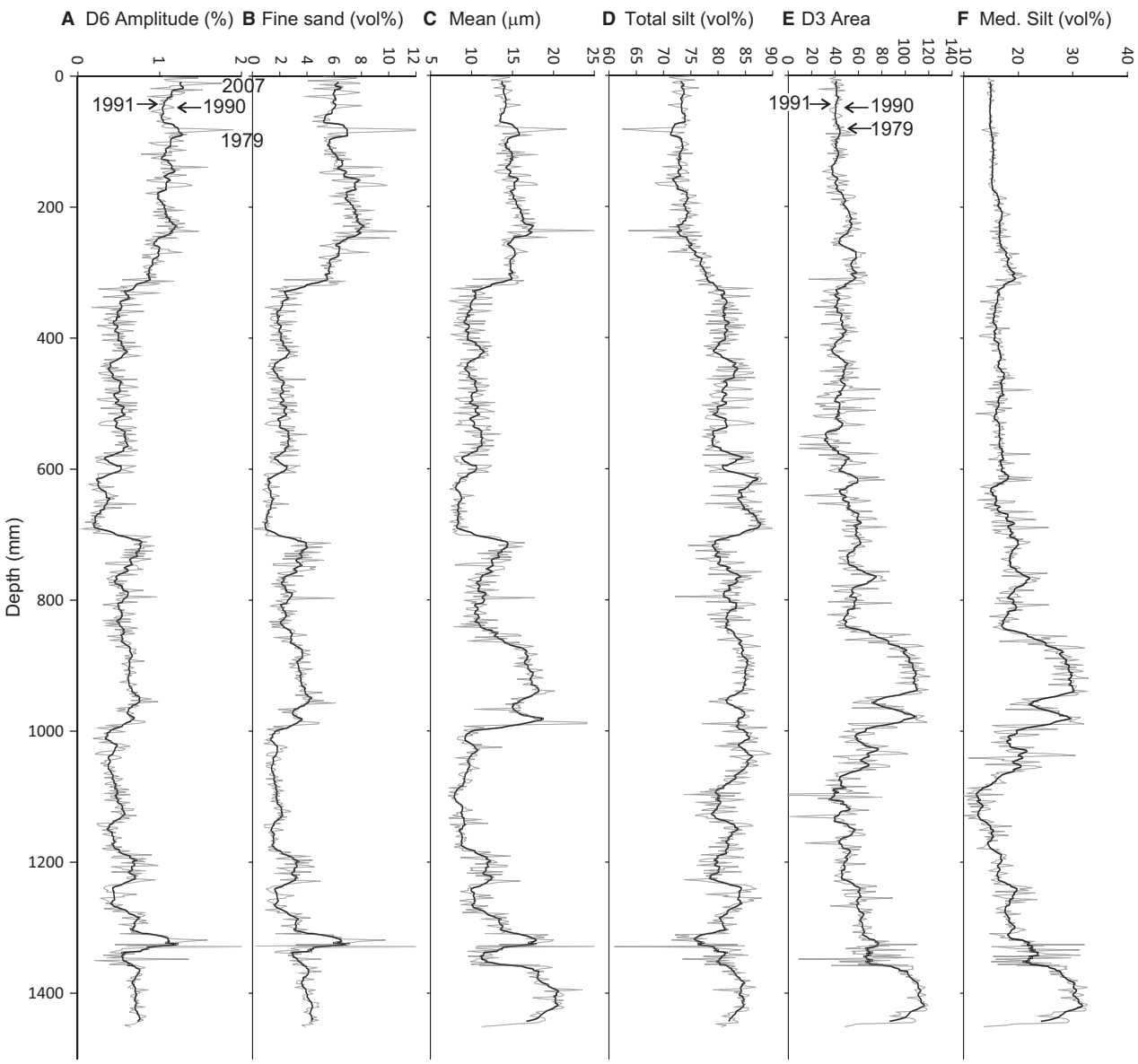


**Fig. 6.** Variation with depth down core of selected variables: (A) D6 Amplitude – note the large spikes at various positions down core, and the ages of different peaks (discussed in text); (B) fine sand; (C) mean grain size; (D) total silt; (E) D3 Area; and (F) medium silt. Grey lines are the individual measurements and the black line represents a nine-point moving average. D3 Area and D6 Amplitude are the complete data as extrapolated by the polynomial algorithm from the training set.

considerably worse than just medium silt, primarily because of the strong overlap with D2 in the fine silt range. Interestingly, total silt correlates better, but in a negative sense, with D6 Amplitude. This is probably an effect of the statistical closure of the raw class-size data (*sensu* Atkinson, 1986), whereby the sand component (mainly D6 because D5 is small) plus the total silt component (D2 to D4) sum to near 100% (the D1 clay population being, like D5, a relatively small component of the system).

There is a relatively high correlation between mean grain size and D6 Amplitude, and a weak, but statistically significant, correlation between mean grain size and D3 Area (Table 3, Figs 6A, 6C, 6E and 7B). The D6 population, despite having lower amplitude than D3, occurs across a much broader range of grain sizes (a range of *ca* 125 μm for D6 compared to *ca* 30 μm for D3). Therefore, D6 is generally the larger of the two populations with a commensurately higher impact on the mean grain size. Nonetheless, the

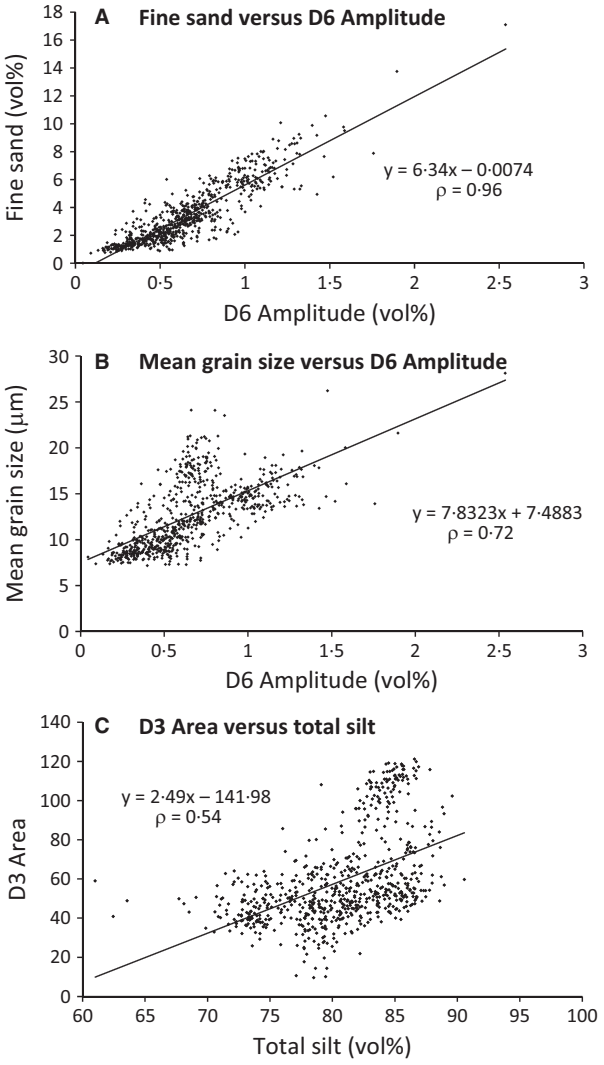


**Fig. 7.** Cross-plots with regression equations of selected variables from Fig. 6: (A) Fine sand versus D6 Amplitude, which is an example of a good, although unlikely, correlation; (B) mean grain size versus D6 Amplitude. For D6 Amplitude <0·7, the data are highly scattered, indicating the region where the mean grain size is probably a composite variable of other grain-size populations. The reasonable correlation is mostly driven by the higher D6 Amplitude values that have a considerable impact on mean grain size; (C) D3 Area versus Total Silt. No traditional grain-size measure can adequately reproduce the D3 Area data. ρ is the Spearman's rank correlation.

correlation to D3 mean grain size is influenced by both bedload and suspended load components. The bedload to suspended load ratio changes on a sample to sample basis, and consequently mean grain size has no consistent relationship to the depositional processes that operated at ALE.

With careful selection, traditional grain-size class distinctions can provide proxy data that reflect depositional processes (for example, at ALE, the fine sand measure is a good approximation for the D6 bedload population; Fig. 7A; Table 3). However, if the goal of using a grain-size measure is to generate a proxy measure for depositional processes, then traditional summary measures are commonly a composite of different portions of one or more depositional processes. In stratigraphic or time-series studies, such a composite grain-size measure will yield proxy data points that contain variable and non-uniform proportions of different transport–depositional processes. Essentially, this is introducing error into the proxy measure. Whether this error is sufficient to mask the overarching controls within the system, such as climatic forcing, will probably be context-specific.

## CONCLUSIONS

A high-resolution grain-size dataset has been obtained from a 1·45 m freeze core collected from a boreal lake (termed Alberta Lake E 'ALE') in north-eastern Alberta, Canada. A novel approach to deconvolving these data into individual log-normal grain-size populations demonstrates the following:

**1** Automated deconvolution and peak fitting failed to yield sedimentologically realistic results. Combining second and fourth derivative-derived modal constraints with an iterative deconvolution and peak-fitting procedure yielded realistic solutions that were consistent with the structure of the grain-size spectra.

**2** Statistical analysis of the magnitude (area and amplitude), position (mode) and shape (FWHH–full-width at half the height of the maximum amplitude) parameters of the deconvolved log-normal distributions can assist in determining the validity of the procedure and relationships between the different distributions. In this study, positive correlations between the magnitude parameters in the data suggest overarching environmental controls on the processes, while non-correlations between the position (mode) and shape (FWHH) parameters suggest that independent transport–depositional processes are reflected by the extracted log-normal distributions.

**3** Overall, given that there are an infinite number of solutions when deconvolving grain-size spectra and that most stratigraphic grain-size series lack independent data to verify

 

the best solution, this method delivers a more objective and explicit method for prioritizing which spectral parameters deliver the most consistent, statistically defensible and sedimentologically realistic solutions. In this study, the priority information was the modes of the different distributions and the basic spectral structure exhibited throughout the dataset.

Alberta Lake E is situated in a sub-humid, boreal, flat, wetland environment. Sediment delivery to ALE occurs via surface overland flow run-off during spring melt, a function of a flat, frozen, impermeable subsurface that essentially bypasses the high melt volumes. In contrast, the wetlands act as a precipitation and sediment particle sink during the summer growing season. This means:

**4** The consistent grain-size spectral structure throughout the core is probably a reflection of this relatively simple sedimentological context, whereby inorganic grains are only delivered by overland flow during spring snow melt.

**5** Conceptually the grain-size spectra can be interpreted as measures of both the intensity of spring melt (bedload component) and the volume of spring melt (suspended load component). Thus, the discrete and consistent deconvolved grain-size populations can be qualitatively linked to specific environmental processes throughout the stratigraphic series.

**6** Comparison of the deconvolved grain-size populations against traditional measures of grain size (for example, mean grain size and total silt) demonstrates that the traditional measures are generally composites of different grain-size populations that therefore contain a component of random error. Deconvolved populations probably yield better proxy data for time-series and stratigraphic analysis.

**7** Stratigraphic series using two parameters from the deconvolved populations demonstrate that ALE has undergone both long-wavelength and short-wavelength oscillations for both spring-melt intensity and spring-melt volume. Further research could perhaps calibrate and quantify how well these populations capture these spring-melt dynamics.

## ACKNOWLEDGEMENTS

This article comes from the multi-disciplinary Coal and Oil Resources Environmental Sustainability (CORES) Project of the Geological Survey of Canada. Many people in that team have helped to generate different aspects of this project, and while not specifically part of this research, the team approach made this research possible – many thanks for the support. Many thanks also to Lakeshore Helicopters, whose expert pilot got us into ALE and those who take on the heavy administrative load associated with managing a government research project. Four external anonymous reviews helped clarify important aspects of the manuscript. An internal GSC review by Dr Rob Rainbird and editorial contributions by Elizabeth Anderson were highly beneficial for clarifying the text. To the best of all co-authors' knowledge, no co-author has a real, apparent or potential conflict of interest.

## REFERENCES

**Anderson, L.** (2012) Rocky Mountain hydroclimate: Holocene variability and the role of insolation, ENSO, and the North American Monsoon. *Global Planet. Change*, **92–93**, 198–208.

**Andriashek, L.D.** (2003) *Quaternary Geological Setting of the Athabasca Oil Sands (in situ) Area, North East Alberta*. Energy Resources Conservation Board, Alberta Geological Survey, Edmonton, AB, Canada.

**Ashley, G.M.** (1978) Interpretation of polymodal sediments. *J. Geol.*, **86**, 411–421.

**Atkinson, A.C.** (1986) Masking unmasked. *Biometrika*, **73**, 533–541.

**Bagnold, R.A.** and **Barndorff-Nielsen, O.** (1980) The pattern of natural size distributions. *Sedimentology*, **27**, 199–207.

**Bah, A.R.**, **Kravchuk, O.** and **Kirchhof, G.** (2009) Fitting performance of particle-size distribution models on data derived by conventional and laser diffraction techniques. *Soil Sci. Soc. Am. J.*, **73**, 1101–1107.

**Bartholdy, J.**, **Christiansen, C.** and **Pedersen, B.T., Jr.** (2007) Comparing spatial grain-size trends inferred from textural parameters using percentile statistical parameters and those based on the log-hyperbolic method. *Sed. Geol.*, **202**, 436–452.

**Bartholomä, A.** and **Flemming, B.W.** (2007) Progressive grain-size sorting along an intertidal energy gradient. *Sed. Geol.*, **202**, 464–472.

**Barusseau, J.P.** (2011) Influence of mixtures of grain-size populations on the parametric and modal characteristics of Coastal Sands (Hérault, Mediterranean Sea, France). *J. Sed. Res.*, **81**, 611–629.

**Best, J.L.**, **Kostaschuk, R.A.**, **Peakall, J.**, **Villard, P.V.** and **Franklin, M.** (2005) Whole flow field dynamics and velocity pulsing within natural sediment-laden underflows. *Geology [Boulder]*, **33**, 765–768.

**Blott, S.J.** and **Pye, K.** (2001) GRADISTAT; a grain size distribution and statistics package for the analysis of unconsolidated sediments. *Earth Surf. Proc. Land.*, **26**, 1237–1248.

**Campbell, C.** (1998) Late Holocene Lake sedimentology and climate change in Southern Alberta, Canada. *Quatern. Res.*, **49**, 96–101.

**Carson, M.A.**, **Taylor, C.H.** and **Grey, B.J.** (1973) Sediment production in a small Appalachian watershed during spring runoff: the Eaton Basin, 1970-1972. *Can. J. Earth Sci.*, **10**, 1707–1734.

**Chambers, R.L.** and **Eadie, B.J.** (1981) Nepheloid and suspended particulate matter in south-eastern Lake Michigan*. *Sedimentology*, **28**, 439–447.

**Chang, T.S.**, **Joerdel, O.**, **Flemming, B.W.** and **Bartholomä, A.** (2006) The role of particle aggregation/disaggregation in muddy sediment dynamics and seasonal sediment turnover in a back-barrier tidal basin, East Frisian Wadden Sea, southern North Sea. *Mar. Geol.*, **235**, 49–61.

**Chang, T.S.**, **Flemming, B.W.** and **Bartholomä, A.** (2007) Distinction between sortable silts and aggregated particles in muddy intertidal sediments of the East Frisian Wadden Sea, southern North Sea. *Sed. Geol.*, **202**, 453–463.

**Chen, Y.**, **Chen, S.**, **Liu, J.**, **Yao, M.**, **Sun, W.** and **Zhang, Q.** (2013) Environmental evolution and hydrodynamic process of Dongping Lake in Shandong Province, China, over the past 150 years. *Environ. Earth Sci.*, **68**, 69–75.

**Cockburn, J.M.H.** and **Lamoureux, S.F.** (2007) Century-scale variability in late-summer rainfall events recorded over seven centuries in subannually laminated lacustrine sediments, White Pass, British Columbia. *Quatern. Res.*, **67**, 193–203.

**Cockburn, J.M.H.** and **Lamoureux, S.F.** (2008a) Hydroclimate controls over seasonal sediment yield in two adjacent High Arctic watersheds. *Hydrol. Process.*, **22**, 2013–2027.

**Cockburn, J.M.H.** and **Lamoureux, S.F.** (2008b) Inflow and lake controls on short-term mass accumulation and sedimentary particle size in a High Arctic lake: implications for interpreting varved lacustrine sedimentary records. *J. Paleolimnol.*, **40**, 923–942.

**Dietze, E.**, **Hartmann, K.**, **Diekmann, B.**, **Ijmker, J.**, **Lehmkuhl, F.**, **Opitz, S.**, **Stauch, G.**, **Wünnemann, B.** and **Borchers, A.** (2012) An end-member algorithm for deciphering modern detrital processes from lake sediments of Lake Donggi Cona, NE Tibetan Plateau, China. *Sed. Geol.*, **243–244**, 169–180.

**Dietze, E.**, **Wünnemann, B.**, **Hartmann, K.**, **Diekmann, B.**, **Jin, H.**, **Stauch, G.**, **Yang, S.** and **Lehmkuhl, F.** (2013) Early to mid-Holocene lake high-stand sediments at Lake Donggi Cona, northeastern Tibetan Plateau, China. *Quatern. Res.*, **79**, 325–336.

**Fang, X.**, **Pomeroy, J.W.**, **Westbrook, C.J.**, **Guo, X.**, **Minke, A.G.** and **Brown, T.** (2010) Prediction of snowmelt derived streamflow in a wetland dominated prairie basin. *Hydrol. Earth Syst. Sci.*, **14**, 991–1006.

**Fisher, D.A.** (2011) Connecting the Atlantic-sector and the north Pacific (Mt Logan) ice core stable isotope records during the Holocene: the role of El Niño. *Holocene*, **21**, 1117–1124.

**Flemming, B.W.** (2007) The influence of grain-size analysis methods and sediment mixing on curve shapes and textural parameters: implications for sediment trend analysis. *Sed. Geol.*, **202**, 425–435.

**Friedman, G.M.** (1962) On sorting, sorting coefficients, and the lognormality of the grain-size distribution of sandstones. *J. Geol.*, **70**, 737–753.

**Gibson, J.J.**, **Edwards, T.W.D.** and **Prowse, T.D.** (1993) Runoff generation in a high boreal wetland in northern Canada. *Nord. Hydrol.*, **24**, 213.

**Gray, D.M.**, **Toth, B.**, **Zhao, L.**, **Pomeroy, J.W.** and **Granger, R.J.** (2001) Estimating areal snowmelt infiltration into frozen soils. *Hydrol. Process.*, **15**, 3095–3111.

**Hajek, E.A.**, **Huzurbazar, S.V.**, **Mohrig, D.**, **Lynds, R.M.** and **Heller, P.L.** (2010) Statistical characterization of grain-size distributions in sandy fluvial systems. *J. Sed. Res.*, **80**, 184–192.

**Hamilton, D.** and **Mitchell, S.** (1996) An empirical model for sediment resuspension in shallow lakes. *Hydrobiologia*, **317**, 209–220.

**Hamm, N.T.** and **Dade, W.B.** (2013) A laboratory study of dynamic sorting of fine, non-cohesive particles by steady, unidirectional currents. *Mar. Geol.*, **336**, 215–222.

**Hartmann, D.** (2007) From reality to model: operationalism and the value chain of particle-size analysis of natural sediments. *Sed. Geol.*, **202**, 383–401.

**van Hengstum, P.J.**, **Reinhardt, E.G.**, **Boyce, J.I.** and **Clark, C.** (2007) Changing sedimentation patterns due to historical land-use change in Frenchman's Bay, Pickering, Canada: evidence from high-resolution textural analysis. *J. Paleolimnol.*, **37**, 603–618.

**Hofmann, H.**, **Lorke, A.** and **Peeters, F.** (2008) The relative importance of wind and ship waves in the littoral zone of a large lake. *Limnol. Oceanogr.*, **53**, 368.

**Holz, C.**, **Stuut, J.-B.W.**, **Henrich, R.D.** and **Meggers, H.** (2007) Variability in terrigenous sedimentation processes off northwest Africa and its relation to climate changes: inferences from grain-size distributions of a Holocene marine sediment record. *Sed. Geol.*, **202**, 499–508.

**Ijmker, J.**, **Stauch, G.**, **Dietze, E.**, **Hartmann, K.**, **Diekmann, B.**, **Lockot, G.**, **Opitz, S.**, **Wünnemann, B.** and **Lehmkuhl, F.** (2012) Characterisation of transport processes and sedimentary deposits by statistical end-member mixing analysis of terrestrial sediments in the Donggi Cona lake catchment, NE Tibetan Plateau. *Sed. Geol.*, **281**, 166–179.

**Jautzy, J.**, **Ahad, J.M.E.**, **Gobeil, C.** and **Savard, M.M.** (2013) Century-long source apportionment of PAHs in Athabasca Oil Sands Region Lakes using diagnostic ratios and compound-specific carbon isotope signatures. *Environ. Sci. Technol.*, **47**, 6155–6163.

**Jin, K.** and **Ji, Z.** (2004) Case study: modeling of sediment transport and wind-wave impact in Lake Okeechobee. *J. Hydraul. Eng.*, **130**, 1055–1067.

**Johnson, T.C.** and **McCave, I.N.** (2008) Transport mechanism and paleoclimatic significance of terrigenous silt deposited in varved sediments of an African rift lake. *Limnol. Oceanogr.*, **53**, 1622–1632.

**Kranck, K.**, **Smith, P.C.** and **Milligan, T.G.** (1996a) Grain-size characteristics of fine-grained unflocculated sediments 11: "multi-round" distributions. *Sedimentology*, **43**, 597–606.

**Kranck, K.**, **Smith, P.C.** and **Milligan, T.G.** (1996b) Grain-size characteristics of fine-grained unflocculated sediments; I, 'One-round' distributions. *Sedimentology*, **43**, 589–596.

**Kværner, J.** and **Kløve, B.** (2008) Generation and regulation of summer runoff in a boreal flat fen. *J. Hydrol.*, **360**, 15–30.

**Laudon, H.**, **Sjöblom, V.**, **Buffam, I.**, **Seibert, J.** and **Mörth, M.** (2007) The role of catchment scale and landscape characteristics for runoff generation of boreal streams. *J. Hydrol.*, **344**, 198–209.

**Law, B.A.**, **Hill, P.S.**, **Milligan, T.G.**, **Curran, K.J.**, **Wiberg, P.L.** and **Wheatcroft, R.A.** (2008) Size sorting of fine-grained sediments during erosion: results from the western Gulf of Lions. *Cont. Shelf Res.*, **28**, 1935–1946.

**Le Roux, J.P.** and **Rojas, E.M.** (2007) Sediment transport patterns determined from grain size parameters: overview and state of the art. *Sed. Geol.*, **202**, 473–488.

**Leys, J.**, **McTainsh, G.**, **Koen, T.**, **Mooney, B.** and **Strong, C.** (2005) Testing a statistical curve-fitting procedure for quantifying sediment populations within multi-modal particle-size distributions. *Earth Surf. Proc. Land.*, **30**, 579–590.

**Luettich, R.A.**, **Harleman, D.R.** and **Somlyody, L.** (1990) Dynamic behavior of suspended sediment concentrations in a shallow lake perturbed by episodic wind events. *Limnol. Oceanogr.*, **35**, 1050–1067.

**Lwin, T.** (2003) Parameterization of particle size distributions by three methods. *Math. Geol.*, **35**, 719–736.

**Lyon, S.W.**, **Nathanson, M.**, **Spans, A.**, **Grabs, T.**, **Laudon, H.**, **Temnerud, J.**, **Bishop, K.H.** and **Seibert, J.** (2012) Specific discharge variability in a boreal landscape. *Water Resour. Res.*, **48**, W08506.

**Macumber, A.L.**, **Patterson, R.T.**, **Neville, L.A.** and **Falck, H.** (2011) A sledge microtome for high resolution subsampling of freeze cores. *J. Paleolimnol.*, **45**, 307–310.

**McCave, I.N.** and **Hall, I.R.** (2006) Size sorting in marine muds; processes, pitfalls, and prospects for paleoflow-speed proxies. *Geochem. Geophys. Geosyst.*, **7**, Q10N05.

**McCave, I.N.**, **Manighetti, B.** and **Beveridge, N.A.S.** (1995a) Circulation in the glacial North Atlantic inferred from grain-size measurements. *Nature*, **374**, 149–152.

**McCave, I.N.**, **Manighetti, B.** and **Robinson, S.G.** (1995b) Sortable silt and fine sediment size/composition slicing: parameters for palaeocurrent speed and palaeoceanography. *Paleoceanography*, **10**, 593–610.

**McConnachie, J.L.** and **Petticrew, E.L.** (2006) Tracing organic matter sources in riverine suspended sediment: implications for fine sediment transfers. *Geomorphology*, **79**, 13–26.

**McDonald, D.M.** and **Lamoureux, S.F.** (2009) Hydroclimatic and channel snowpack controls over suspended sediment and grain size transport in a High Arctic catchment. *Earth Surf. Proc. Land.*, **34**, 424–436.

**McDonald, D.M.**, **Lamoureux, S.F.** and **Warburton, J.** (2010) Assessment of a time-integrated fluvial suspended sediment sampler in a high arctic setting. *Geogr. Ann. Ser. A Phys. Geogr.*, **92**, 225–235.

**McLaren, P.** and **Bowles, D.** (1985) The effects of sediment transport on grain-size distributions. *J. Sed. Res.*, **55**, 457–470.

**McLaws, I.J.** (1980) Silica sands in the Fort McMurray area, Alberta. In: *Economic Geology Report 6* (Ed. A.R. Council), Government of Alberta, Edmonton, Alberta, 61 pp.

**McNamara, J.P.**, **Chandler, D.**, **Seyfried, M.** and **Achet, S.** (2005) Soil moisture states, lateral flow, and streamflow generation in a semi-arid, snowmelt-driven catchment. *Hydrol. Process.*, **19**, 4023–4038.

**Metcalfe, R.A.** and **Buttle, J.M.** (1999) Semi-distributed water balance dynamics in a small boreal forest basin. *J. Hydrol.*, **226**, 66–87.

**Metcalfe, R.A.** and **Buttle, J.M.** (2001) Soil partitioning and surface store controls on spring runoff from a boreal forest peatland basin in north-central Manitoba, Canada. *Hydrol. Process.*, **15**, 2305–2324.

**Middleton, G.V.** (1976) Hydraulic interpretation of sand size distributions. *J. Geol.*, **84**, 405–426.

**Middleton, G.V.** (1990) Fitting cumulative curves using splines. *J. Sed. Res.*, **60**, 615–616.

**Molinaroli, E.**, **Guerzoni, S.**, **De Falco, G.**, **Sarretta, A.**, **Cucco, A.**, **Como, S.**, **Simeone, S.**, **Perilli, A.** and **Magni, P.** (2009) Relationships between hydrodynamic parameters and grain size in two contrasting transitional environments: the Lagoons of Venice and Cabras, Italy. *Sed. Geol.*, **219**, 196–207.

**Murray, M.R.** (2002) Is laser particle size determination possible for carbonate-rich lake sediments? *J. Paleolimnol.*, **27**, 173–183.

PAGES_2k_Consortium (2013) Continental-scale temperature variability during the past two millennia. *Nat. Geosci.*, **6**, 339–346.

**Påsse, T.** (1997) Grain size distribution expressed as tanh-functions. *Sedimentology*, **44**, 1011–1014.

**Poizot, E.**, **Méar, Y.** and **Biscara, L.** (2008) Sediment trend analysis through the variation of granulometric parameters: a review of theories and applications. *Earth Sci. Rev.*, **86**, 15–41.

**Pomeroy, J.W.**, **Gray, D.M.**, **Brown, T.**, **Hedstrom, N.R.**, **Quinton, W.L.**, **Granger, R.J.** and **Carey, S.K.** (2007) The cold regions hydrological model: a platform for basing process representation and model structure on physical evidence. *Hydrol. Process.*, **21**, 2650–2667.

**Qin, X.**, **Cai, B.** and **Liu, T.** (2005) Loess record of the aerodynamic environment in the East Asia monsoon area since 60,000 years before present. *J. Geophysi. Res. Solid Earth*, **110**, B01204.

**Redding, T.E.** and **Devito, K.J.** (2008) Lateral flow thresholds for aspen forested hillslopes on the Western Boreal Plain, Alberta, Canada. *Hydrol. Process.*, **22**, 4287–4300.

**Redding, T.** and **Devito, K.** (2011) Aspect and soil textural controls on snowmelt runoff on forested Boreal Plain hillslopes. *Hydrol. Res.*, **42**, 250–267.

Seasolve (2003) *PeakFit: v4 Users Guide*. Seasolve Software Inc., Massachusetts, 255 pp.

**Sheridan, M.F.**, **Wohletz, K.H.** and **Dehn, J.** (1987) Discrimination of grain-size subpopulations in pyroclastic deposits. *Geology*, **15**, 367–370.

**Shook, K.**, **Pomeroy, J.W.**, **Spence, C.** and **Boychuk, L.** (2013) Storage dynamics simulations in prairie wetland hydrology models: evaluation and parameterization. *Hydrol. Process.*, **27**, 1875–1889.

**Singer, J.K.** and **Anderson, J.B.** (1984) Use of total grain-size distributions to define bed erosion and transport for poorly sorted sediment undergoing simulated bioturbation. *Mar. Geol.*, **57**, 335–359.

**Slattery, M.C.** and **Burt, T.P.** (1997) Particle size characteristics of suspended sediment in hillslope runoff and stream flow. *Earth Surf. Proc. Land.*, **22**, 705–719.

**Sonnenburg, E.P.**, **Boyce, J.I.** and **Reinhardt, E.G.** (2013) Multi-proxy lake sediment record of prehistoric (Paleoindian-Archaic) archaeological paleoenvironments at Rice Lake, Ontario, Canada. *Quatern. Sci. Rev.*, **73**, 77–92.

**Soulsby, R.L.**, **Hamm, L.**, **Klopman, G.**, **Myrhaug, D.**, **Simons, R.R.** and **Thomas, G.P.** (1993) Wave-current interaction within and outside the bottom boundary layer. *Coast. Eng.*, **21**, 41–69.

**Sun, D.**, **Bloemendal, J.**, **Rea, D.K.**, **Vandenberghe, J.**, **Jiang, F.**, **An, Z.** and **Su, R.** (2002) Grain-size distribution function of polymodal sediments in hydraulic and aeolian environments, and numerical partitioning of the sedimentary components. *Sed. Geol.*, **152**, 263–277.

**Syvitski, J.P.M.** (1991) *Principles, Methods, and Application of Particle Size Analysis*. Cambridge Univ. Press, New York.

**Tanner, W.F.** (1964) Modification of sediment size distributions. *J. Sed. Res.*, **34**, 156–164.

**Tanner, W.F.** (1983) Hydrodynamic origin of Gaussian size distribution. *Proc. Symp. Coastal Sed.*, **6**, 12–34.

**Wang, H.**, **Mason, J.A.** and **Balsam, W.L.** (2006) The importance of both geological and pedological processes in control of grain size and sedimentation rates in Peoria Loess. *Geoderma*, **136**, 388–400.

**Weltje, G.J.** and **Prins, M.A.** (2003) Muddled or mixed? Inferring palaeoclimate from size distributions of deep-sea clastics. *Sed. Geol.*, **162**, 39–62.

**Weltje, G.J.** and **Prins, M.A.** (2007) Genetically meaningful decomposition of grain-size distributions. *Sed. Geol.*, **202**, 409–424.

**Xiao, J.**, **Chang, Z.**, **Fan, J.**, **Zhou, L.**, **Zhai, D.**, **Wen, R.** and **Qin, X.** (2012) The link between grain-size components and depositional processes in a modern clastic lake. *Sedimentology*, **59**, 1050–1062.

**Young, I.R.** and **Verhagen, L.A.** (1996) The growth of fetch limited waves in water of finite depth. Part 1. Total energy and peak frequency. *Coast. Eng.*, **29**, 47–78.

*Manuscript received 1 May 2015; revision accepted 25 February 2016*

## Supporting Information

Additional Supporting Information may be found in the online version of this article:

**Figure S1.** Map of the landscape around ALE. The half-toned green shading indicates the mapped wetlands surrounding ALE. A stand of lodgepole pine vegetation in the north-eastern quadrant of ALE was not captured in the mapping, probably because it was too small to capture at the 1:250,000 map scale of the data. Orange dot within ALE is the approximate coring location. Yellow lines are 10 m spaced contours with some contours numbered to indicate their height in metres above sea-level (masl). Blue lines are water courses, with the Steepbank and Clearwater Rivers noted. Data from "Canvec" map series (available free at http://geogratis.gc.ca/api/en/nrcan-rncan/esssst/9e555875-628f-4bb2-9c25-67e2b94252e9.html).

**Figure S2.** The sedimentological context of ALE. (A) Photograph looking west north-westward to the western end of ALE. The lake is surrounded by a large glacial terrace dominated by scrubby, dense spruce-tamarack forest (the tamarack can be identified through its yellow-coloured, autumn leaves). The lake shore is rimmed by a floating fen of graminoids and horsetails (*Equisetum* sp.). The sole inlet creek entering ALE has built a small bay-head delta. The Firebag Hills Uplands are visible towards the top of the photograph and represent the highest topography in the region, forming part of the headwaters for the Clearwater River. Photograph courtesy of Dr. Jason Ahad. (B) 1990 to 1991 daily streamflow hydrograph for the "Clearwater above Christina" hydrometric station, situated approximately 20 km down river from ALE. The 1990 year annual hydrographic profile has a single large spring-melt peak and minimal summer storm-related high discharge events (NB. the 1990 spring melt was above the average spring discharge of *ca* 150 $m^3$ $s^{-1}$; see inset panel C). The 1991 annual hydrograph has a small spring-melt discharge and a large summer storm peak discharge. 1990 is a typical year, 1991 is atypical, in particular the very high summer storm peak (which is close to the historical high for June discharge at this hydrometric station). For both years, the discharge profile indicates that high discharge events take some months to fully decay back to baseline flow. Grey boxes denote nival discharge period, curved arrows denote recession from peak to base flow conditions. (C) Compiled average, minimum and maximum streamflow data for the 46-year Christina hydrometric record. However, note from (B) that the timing of peak spring-melt discharge can occur from April to June, which biases month-based long-term averages, maximums and minimums.

**Figure S3.** (A) and (B) Evolution of the grain-size spectra using different treatments. (A) Firstly no treatment (original 'O' spectrum), then gentle ultrasonic (U spectrum) and finally gentle ultrasonic plus metaphosphate (U+P spectrum). (B) Similar to (A) except treatments reversed with firstly O, then P and finally U + P. Discussed in supplementary text. (C) Grains from 1330 mm depth sample. Typical Photomicrograph of typical residue after grain-size analysis, showing angular to rounded detrital grains, predominantly silt (throughout background) with minor sand grains that are mostly lithic fragments (black arrow highlights an angular clastic mudstone grain) and minor quartz (white arrow, this one is rounded, but grains range from angular to rounded). (D) Grain from 1340 mm depth sample. Grains showing cleavage fracture consistent with carbonate that were interpreted as such during microfossil examination. Both (C) and (D) are grains captured post-laser particle analysis from samples with no metaphosphate or ultrasonic treatment. Black lines represent 100 mm scale in both (C) and (D).

**Figure S4.** Examples of alternative deconvolutions of these spectra, which can be compared against the constrained solutions for the same samples in Figure 2. (A) Fully automated deconvolution and peak fitting. Only two distributions found, with modes at 8·3 mm and 117·6 mm. Dotted line is the measured data, and solid line is the summed model data for the two distributions (small dashes). Large dashed lines represent 99 percent confidence limits that include all measured data points. Fit statistics are satisfactory, but not as excellent as for other solutions. (B) Unconstrained model that produces a dominant very fine silt distribution 2 whose shoulders extend across the whole measured grain-size range. The mode of this distribution is significantly coarser than that for unambiguous distribution 2 peaks (5 to 6·5 μm). The fine silt distribution 3 is highly subdued and thus does not well reflect the unambiguous fine silt peak present in this overall coarser-grained sample (i.e. this fit is poor for samples with unambiguous distribution 3 peaks and is considered significantly worse for finer-grained samples that have a single peak in the 3 to 30 μm range). The peak fit places both distributions 4 and 5 into the 40 to 60 μm range, which is not representative of the basic structure of the spectra. C) An

 

alternative to constraining mode 2 to 5–6.5 μm is to constrain mode 3 to 17–20 μm, the range it exhibits in samples with unambiguous distribution 3 peaks. In finer-grained samples, this tends to generate a large distribution 2 with a mode 2 that is much coarser-grained than mode 2 in samples that have an unambiguous distribution 2 peak. Distribution 3 is reduced in size in such solutions, and overall, this constraint leads to models that are similar to unconstrained models for this grain-size range.

**Figure S5.** Stack of 29 grain-size spectra from 495 to 551 mm depth in ALE core. This stack demonstrates both the uniformity of the basic spectral structure and the cyclic nature of sedimentation patterns in ALE from coarser-grained (solid lines) to finer-grained (dotted lines) spectra with intermediate spectra in some cycles (dashed lines). The apparent cyclicity is designated by the 1 to 5 numerals at right. Note that the cycles are arbitrarily defined on a finer-grained and coarser-grained transition and that the cycle numbering is not meant to imply that this represents the only possible cyclic phenomena present in this section of the core, for example, there could be cycles on shorter length scales than the 2 mm sampling resolution. The volume percent scale for all spectra is top right. Fig. 2 presents the deconvolution of the 505 to 509 spectra.

**Data S1.** Raw data

**Table S1.** Pearson correlation coefficients ($r^2$) and regression slopes between unconstrained and constrained solutions for area, amplitude, mode and FWHH

**Appendix S1.** Derived polynomial equations for D6 Amplitude and D3 Area. The term [GSC#] refers to the Grain Size Class measurement for that sample, for example, GSC101 is the measurement for the grain-size class centred on 101 μm.